Available online at www.sciencedirect.com

SciVerse ScienceDirect

Acta Materialia 60 (2012) 4311–4318

Acta MATERIALIA

www.elsevier.com/locate/actamat

Observation of recovery and recrystallization in high-purity aluminum measured with forward modeling analysis of high-energy diffraction microscopy

Christopher M. Hefferan [a], Jonathan Lind [a], Shiu Fai Li [a], Ulrich Lienert [b], Anthony D. Rollett [c], Robert M. Suter [a,*]

[a] Department of Physics, Carnegie Mellon University, Pittsburgh, PA 15213, USA
[b] Advanced Photon Source, Argonne National Laboratory, 9700 South Cass Avenue, Argonne, IL 60439, USA
[c] Department of Materials Science and Engineering, Carnegie Mellon University, Pittsburgh, PA 15213, USA

Received 3 February 2012; received in revised form 12 April 2012; accepted 15 April 2012

Abstract

High-energy X-ray diffraction microscopy is a non-destructive materials characterization technique that is capable of tracking the evolution of three-dimensional microstructures as they respond to external stimuli. We present measurements of the annealing response of high-purity aluminum using the near-field variant of this technique. The data are analyzed with the forward modeling method which produces orientation maps that exhibit complex intragranular structures. Analysis and verification of results use both reconstructed sample space maps and detector space intensity patterns. Sensitivity to the ordering of the microstructure through both recovery and recrystallization is demonstrated. Sharpening of diffraction peaks and a corresponding reduction in intragranular orientation variations signal recovery processes. The emergence of a new bulk grain (recrystallization) is observed in a disordered region of the microstructure; the new grain has an orientation with no obvious relation to those of grains surrounding the disordered region.

Keywords: Microstructure; Recovery; Recrystallization; X-ray diffraction; Forward modeling

1. Introduction

The annealing response of deformed microstructures can be separated into three classes of process, namely recovery, recrystallization and grain growth [1]. Distinct in their specific mechanisms and final state characteristics, all three stages use thermal energy to evolve a polycrystal through a sequence of increasingly ordered states. The available energy allows local changes in dislocation density during recovery, the nucleation of new grains in recrystallization, and the motion of grain boundaries to reduce total interfacial area during grain growth or coarsening. In practice, all three responses can be present concurrently. Study of these stages of annealing is a mature field and has been exhaustively analyzed from both theoretical and experimental perspectives. Nevertheless, the ability to directly observe these responses within bulk material has not been possible due to the limitations of available instrumentation. Now, with the advent of non-destructive synchrotron-based microstructure characterization techniques, observations of internal polycrystal responses to external stimuli are possible [2–9].

While all three classes of annealing response have been studied with synchrotron X-ray techniques, we focus here on recovery and recrystallization. Existing observations [10–16] clearly establish the importance of detailed, non-destructive probes. These studies, however, are limited to the tracking of small numbers of Bragg peaks or lack information regarding the microstructural neighborhood of the monitored grains. We present a three-state, in situ annealing experiment using a polycrystalline wire of high-purity (99.999%) aluminum. The measurement, conducted at the

* Corresponding author. Tel.: +1 412 268 2982; fax: +1 412 681 0648.
E-mail address: suter@andrew.cmu.edu (R.M. Suter).

1359-6454/$36.00 © 2012 Acta Materialia Inc. Published by Elsevier Ltd. All rights reserved.
http://dx.doi.org/10.1016/j.actamat.2012.04.020

Advanced Photon Source (APS) beamline 1-ID, uses near-field high-energy X-ray diffraction microscopy (nf-HEDM) [2–4] to map crystallographic orientations over a volume of material containing thousands of distinguishable orientations. Through subtle, low-temperature annealing, we observe recovery as ordering within existing domains of similar orientation ("grains") and recrystallization as the emergence of new measurable orientations from regions of relatively high disorder.

nf-HEDM [2–4] is used to generate 2-D maps of crystallographic orientations with ~5 μm spatial and 0.1° orientation resolution. The maps can be extended to three dimensions by measuring consecutive cross-sections in a process analogous to 3-D electron backscatter diffraction microscopy (EBSD) surface measurements [17]. Unlike 3-D EBSD, nf-HEDM is non-destructive and therefore allows for the repeated measurement of the same volume of microstructure as it evolves when subjected to external stimuli. The measurement is based on high-resolution imaging of Bragg scattering from individual crystals in a monochromatic, rotating sample scheme. Images are collected in transmission as the sample is rotated about the normal to a line-focused high-energy beam. The rotation is parameterized as ω and images are integrated over an interval $\delta\omega$. The near-field distinction refers to the distance between sample and X-ray detector where the diameter of the specimen is of the same order of magnitude as the sample-to-detector distance. At this length scale, the position of diffraction peaks on the detector is determined by the combination of diffracted beam propagation direction and the position of origin in the sample.

The conversion of thousands of detector images to real space maps of the crystallographic orientation field is accomplished using the forward modeling method [3,18–20]. This method uses a computer simulation to optimize the agreement between experimental data and simulated scattering from crystallographic orientations assigned to a finely gridded tessellation of the sample space. This discretization of sample space, on a length scale much smaller than the grain size, leads to measurement sensitivity to intragranular orientation variations. Specifically, the forward modeling reconstruction connects each sample space volume element (reconstruction mesh element or voxel) with many Bragg reflections in the 4-D detector space, parameterized by pixel addresses on the detector images, j, k, the rotation axis-to-detector distance, L, and the rotation interval position, ω. In the present work, the sample, with its complex intragranular orientation fields, generates detector images of diffracted beams that are similarly complex and difficult to interpret on a one-by-one basis. We illustrate the efficacy of correlating sample space and detector space representations.

2. Experimental procedure

The aluminum specimen was a cylindrical wire measuring 1 mm in diameter and 30 mm in length. Since the wire was formed by drawing, the microstructure had appreciable defect content. In situ annealing was accomplished using a fabricated boron nitride (BN) receptacle, with a 10 mm length of the sample embedded. The BN was resistively heated. The measured volume of microstructure was in air, approximately 19 mm from the BN, and therefore subject to a thermal gradient, though the sampled region was small enough to be approximated by a uniform temperature. The initial state was measured as received, with no thermal treatment. The two annealing treatments achieved temperatures of ~50 and ~70 °C, respectively, after 10 °C incremental steps over ~2.25 h. These temperatures are approximate since calibration of temperature at the measurement position was performed after the measurement. The HEDM data collection consisted of the measurement of 11 2-D cross-sections with 20 μm spacings along the wire axis. Consistent mapping of the same 11 layers was achieved by monitoring the intersection of the line-focused X-ray beam with the sample tip, using a diode detector situated ~2 m downstream of the sample. The sample returned to within a few microns of its initial position after both anneals, permitting repeatable measurement of the same volume of microstructure. In-plane alignment of data sets by a few microns optimized overlap of the different states.

Diffraction data were collected at an operating energy of 50.1 keV. The line-focused beam is <6 μm high and 1.3 mm wide, and therefore an entire cross-section of the cylindrical sample is illuminated. Diffraction spots are imaged at three rotation axis-to-detector distances of $L = 5.1, 7.1$ and 9.1 mm. The detector system was comprised of a lens-coupled CCD camera with a 4.2 mm square field of view of a thin Ce-doped surface scintillation layer on a YAG single crystal. The effective pixel size is 4.11 μm. At each L distance, a series of 100 diffraction images were collected as the sample rotated over $\delta\omega = 1°$ intervals. These images are split between two contiguous 50° regions, with the centers offset by 90°. This set of intervals permits sufficient sampling of spot geometries for spatial reconstruction and spot locations for orientation determination. Good signal-to-noise was observed for scattering up to the {440} family of Bragg peaks.

The reconstruction of the nf-HEDM diffraction data is accomplished with the forward modeling method, which assigns an orientation field to each X-ray-defined sample layer. The forward modeling software [3,18–20] tessellates the sample space with a grid of equilateral triangles. Simulated scattering from each voxel is compared to observed scattering as orientation space is searched. Thus, each voxel is optimized against the complete data set. Broad coverage of ω leads to isotropic orientation and spatial resolution as well as signal averaging of noisy and weak scattering. Over the measured range of ω, arbitrary orientations generate ≈35 distinct Bragg peaks and the optimization in each voxel is based on comparison with the complete set.

3. Results

Reconstructions of a single microstructure layer (the center layer of the measured volume) in each of the three anneal states are shown in Fig. 1. The reconstructions use a uniform grid of 5.1 μm-sided equilateral triangles with each triangle assigned an orientation independently of its neighbors. This mesh size has been selected to approximate the size of detector pixels, which limits the spatial resolution of the measurement. Moderate- to high-angle grain boundaries are visible as boundaries between regions of visibly distinct color. Such boundaries with misorientation angle, $\theta_b \geqslant 2°$, are decorated by the black lines in the figure. Since these lines are determined locally (from nearest-neighbor voxel misorientations), the fact that narrow and continuous lines enclose uniformly colored regions indicates that the noise level or uncertainty in determining the boundary locations is at or below the grid resolution of the reconstruction. Since most uniformly colored regions contain no black lines, very few internal nearest-neighbor voxels are determined to have orientations that differ by as much as 2°. Note, however, that regions that appear to be uniform in color are not necessarily uniform in orientation since the color scale is too coarse to visualize small variations.

Also shown in Fig. 1 are maps of the confidence metric, C. Confidence is defined for each voxel as the fraction of simulated Bragg peaks generated by the optimized orientation that overlap observed diffraction at more than one detector distance, L [3]. Only voxels with $C \geqslant 0.25$ are considered to have converged to a (reasonably) reliable orientation and are included in Fig. 1.

Examination of Fig. 1a–c demonstrates that most boundaries with $\theta_b \geqslant 2°$ exhibit little motion during annealing and that the measurement (both sample alignment and reconstruction) is reproducible to the resolution of the grid. Careful examination does reveal some subtle boundary motions and the emergence of a few new orientations. We conclude that only minimal grain growth or coarsening occurs during this measurement. On the other hand, Fig. 1d–f exhibits increasing average values of C with numerous regions of low confidence disappearing in the final state. The low C regions are predominantly along grain boundaries and in the vicinity of triple lines. Many of the regions extend to neighboring layers and the same ordering trends are visible in all measured layers. Regions with low C appear to be regions of high disorder in which the orientation within our reconstruction voxel length scale varies appreciably, yielding broad and weak scattering. The reconstruction algorithm tends to extend the domain of nearby orientations but with significantly reduced overlap between simulated and experimental peaks. As annealing proceeds, these regions become more ordered, the scattering becomes stronger, and better orientation information is obtained. Below, we discuss details of the orientation and confidence maps in order to extract information about recovery and recrystallization processes that underlie the observed evolution. We compare simulated scattering directly to measured signals in order to corroborate subtle features and trends.

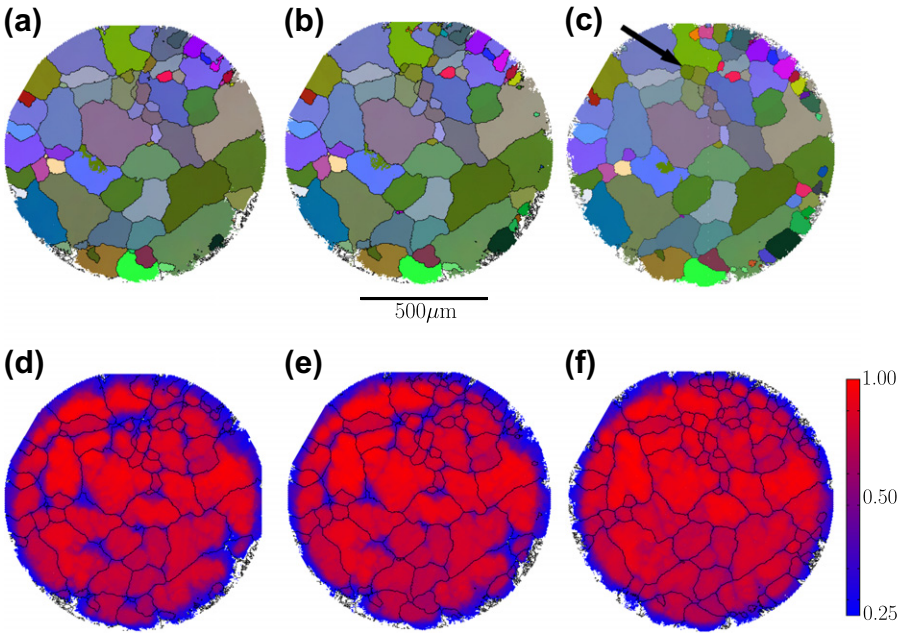

Fig. 1. Maps of the center layer of the measured volume. (a–c) Show orientation maps in the initial, ~50 °C and ~70 °C anneal states, respectively. Each mesh triangle, or voxel, is colored by mapping orientation components (Rodrigues vector representation) to the red–green–blue (RGB) color space. Black lines are drawn between adjacent triangles that have misorientations ⩾2°. (d–f) Show maps of the confidence metric, C, corresponding to the orientation maps in (a)-(c) with the same black lines included. The confidence maps are plotted on the same color scale. $C = 1$ (red) means that ≈35 simulated Bragg peaks overlap observed scattering. The arrow in (c) indicates the nucleated grain discussed in Section 3.2.

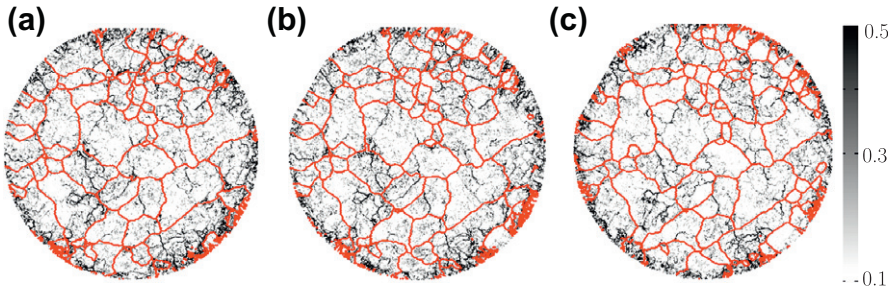

Fig. 2. Kernel-averaged misorientation (KAM) maps of the same three layers of microstructure shown in Fig. 1. The gray scale saturates at $KAM = 0.1$ (white) and $KAM = 0.5$ (black) degrees. All three maps use the same gray scale.

3.1. Recovery

The recovery process is characterized by changes in dislocation density and distributions that result in the reduction of local orientation variations. Crystal orientation variations correspond to a distribution in the directions of local reciprocal lattice vectors, and therefore recovery is observable as a sharpening of intensity distributions. Similar orientation distributions are conventionally measured in rocking curve measurements in single crystals [21]; in effect, we measure such curves for many crystals using many Bragg peaks for each. In our spatially resolved measurements, as grains move towards more uniform orientations, diffraction peaks appear at shorter ω intervals, have reduced arc lengths on a given detector image, and have more uniform intensity across peak profiles. By using forward modeling's voxel-by-voxel (rather than grain-by-grain) reconstruction, we are able to follow this evolution. Again, this capability relies heavily on the inclusion of many diffraction spots over a wide range of ω and the resultant high spatial and orientational resolution.

Fig. 2 shows a measure of local orientation variation, the kernel-averaged misorientation or KAM [22]. Here, KAM is calculated as the average misorientation between a voxel and its nearest neighbors. Since the in-plane map spatial resolution (5.1 μm) is finer than the layer-to-layer spacing (20 μm), only in-plane contributions are included. In the figures, points with $KAM > 2°$ are suppressed and shown as the grain boundary lines in red.[1] Note the highly expanded gray scale in Fig. 2. All voxels with sub-orientation resolution values ($KAM < 0.1°$) are shown as white, while $0.5° < KAM < 2°$ are black. This scale allows one to pick out regions of relatively high disorder (clusters of dark points) as well as seeing light regions with little short-range disorder. Generally, KAM plots do not necessarily show low gradients in orientation ($\lesssim 0.1°$ over 5 μm). In all three sample states, one can pick out noisy regions as well as ordered 1-D structures that correspond to low-angle boundaries. Some of these boundaries have ends that are disconnected from other boundary lines, implying a smooth orientation gradient around the end point. Many of these features can be correlated across the three anneal states of the sample, thus reinforcing the reliability of the reconstructions. One also sees regions in which ordered structure grows rather dramatically. The near-surface region appears to be particularly active in this behavior, indicating the limitations of recovery studies using surface-based techniques.

While the KAM maps in different anneal states are qualitatively similar, there is an overall lightening of the images as annealing progresses, implying decreased average KAM within the sample. This is illustrated in Fig. 3 as histograms obtained from the entire set of 11 measured layers in each state. The population in the sub-resolution ($<0.1°$) bin grows significantly, while large KAM values decrease in population. This growth of orientational order at short length scales is consistent with expected recovery behavior as noted above.

To more directly tie the KAM trends to the experimental signals, we accumulate statistics on peaks widths in the ω direction ("rocking curves"). To accomplish this we use the scattering generated by the optimized orientation field to identify Bragg peak locations and intensity patterns corresponding to real-space regions defined by the $\geqslant 2°$ boundaries shown in Figs. 1 and 2. Defining these regions to be "grains," we count the number of measured ω intervals (each 1° wide) in which each peak occurs in the experimental images (not in the simulation). The 96 grain cross-sections that maintain roughly constant shapes throughout annealing are chosen and 3022 distinct Bragg peaks are studied. The cross-sections are from three distinct layers separated by 100 μm. The average widths are 3.6, 3.4, 3.1 degrees in the three states. Fig. 4 shows the peak width evolution as seen in histograms of changes in widths between anneal states. The higher population of negative values indicates a statistical sharpening of the scattering. The actual values of the average widths reflect orientation variations but are increased by the inefficiency of the ω rotation in moving reciprocal lattice vectors that are close to that axis through the Bragg condition (as reflected in the Lorentz factor [2]).

3.2. Recrystallization

While recovery is a process defined by subtle, continuous changes, recrystallization is a dramatic (critical)

[1] For interpretation of color in Figs. 2–4, 6, the reader is referred to the web version of this article.

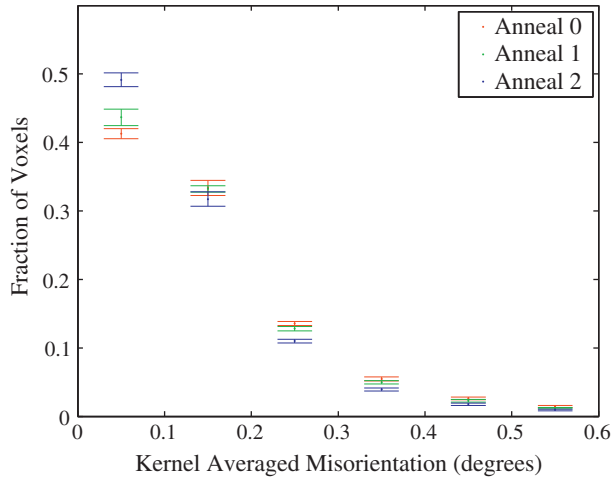

Fig. 3. *KAM* histograms for the three anneal states. Horizontal bin widths are 0.1°. Points are average values of histograms computed for each of the 11 layers and error bars are corresponding standard deviations.

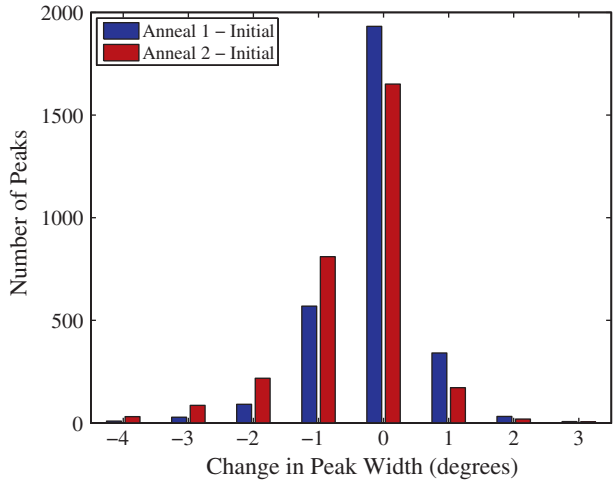

Fig. 4. Histogram of changes in peak widths in experimental detector space as a function of anneal. Each pair of bars refers to changes in the integer numbers of ω intervals in which above background intensity is observed.

microstructural event characterized by the emergence of a new grain or orientation. New grains are detectable by the appearance of new sets of crystallographically consistent Bragg peaks in the 4-D detector space. The size of this space, coupled with its complex population of polycrystalline diffraction peaks, makes identification of new crystals challenging. Using a voxel-based reconstruction, small features can be identified. Post-reconstruction, identification of new grains can be automatically accomplished with point-by-point comparisons of the microstructure in multiple sample states, assuming only subtle motions of grain boundaries. As above, examining scattering that is consistent with the new orientation and its location can link the new grain to its source signal (experimental diffraction) in order to validate its presence and to verify its absence in earlier sample states.

The probed sample volume had a significant number of nucleation events at the surface (see Fig. 1a–c). However, we limit detailed discussion to a single internal grain which is fully contained in our measured volume. The grain is indicated by the arrow in Fig. 1c. Fig. 5 shows the nucleation site in each of the three anneal states. The event occurs in the middle layer of the measured volume. The new orientation is seen in two neighboring layers in the first anneal state, and extends into three adjacent layers (±20 μm displaced) in the final state. Note that the grain emerges from a region with low C in the initial state (Fig. 5d), implying that it nucleated in a highly defected region. In fact, even in the final state, essentially the entire grain occupies this initially defective region. Growth is almost entirely within the deformed region rather than into the neighboring, pre-existing grains. While the new grain grows, the surrounding ones become more ordered as indicated by the more uniformly red C map. Fig. 5g–i shows that the new grain grows with only small internal *KAM*. Evidently, the new grain replaces high-energy–density, disordered material with a low stored energy, ordered crystal structure.

The images of three example peaks shown in Fig. 6 illustrate the evidence for the new grain in the first and final anneal states. The peaks are well defined in ω space, covering only a single (or, in rare cases, a pair of adjacent) $\delta\omega = 1°$ bins. The simulated scattering generated by the voxel-by-voxel optimized orientation is outlined over the experimental intensities. These ω intervals are 3 of 31 where simulated scattering is generated. Of these, 28 are found to overlap experimental scattering, which leads to $C = 0.9$. The initial state is not shown since there is no discernible intensity in the corresponding images. In the two adjacent layers in the final state, weak intensity is observed at each of these locations and is overlapped by simulated scattering. With only three measured cross-sections of this grain, due to the 20 μm layer spacings, a meaningful 3-D grain shape cannot be generated.

We see no clear origin for the orientation of the new grain; this somewhat surprising result [23] is consistent with earlier work by Larsen et al. [15]. No special orientation relations are discernible between the nucleated grain and its neighborhood. Table 1 lists the misorientations in axis-angle form relative to the crystal axes of the new grain. The first six entries are indicated in Fig. 5, while grain 7 is detected in one of the adjacent layers. Grains 1–6 are separated by more than 3° from the nearest coincidence site lattice (CSL) relation; this statement includes CSL numbers as high as 73. Grain 7 has rotation angle close to the Σ23 CSL but the axis is far from the appropriate ⟨3 1 1⟩ direction. Further, we measure no diffraction signals in the initial state at the detector locations struck by the new grain in later states (such as those shown in Fig. 6). Manual examination of raw detector images, without any background treatment, fails to locate intensity peaks at these and other relevant detector positions. Thus, the disordered region where the grain nucleates does not possess

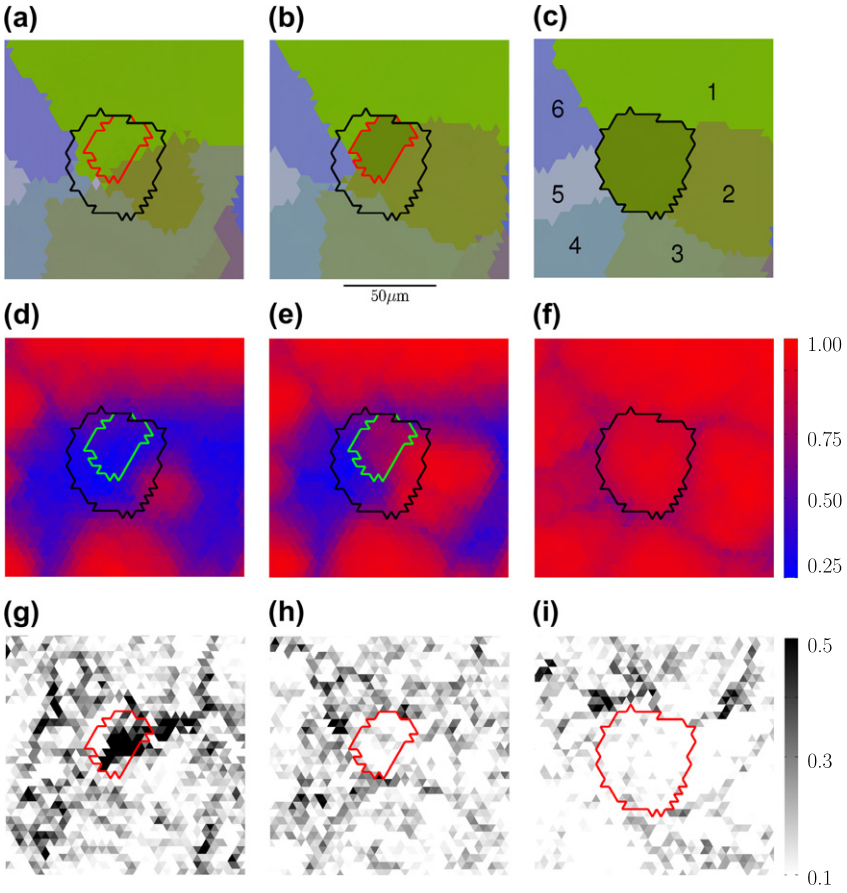

Fig. 5. Maps illustrating the nucleation of a new grain during annealing. Columns from left to right show initial, first and final anneal states. (a–c) Show orientations as in Fig. 1 along with outlines of the new grain as observed in the second and final states. (d–f) Show maps of C in the same region. (g–i) Show KAM values. Misorientations between the nucleated grain and its neighbors are discussed in Section 3.2.

sufficient orientation content at the nucleated grain's value to generate observable experimental signal.

4. Discussion

Simultaneous recovery and recrystallization phenomena are observed in situ in low-temperature (<100 °C) annealing of a high-purity aluminum wire using nf-HEDM. Recovery is evidenced by a statistical sharpening of diffraction peak rocking curves that is reflected in subtle reductions of orientation gradients in real space reconstructions of the orientation field. With orientation resolution of $\approx 0.1°$, subtle changes are observed. Recrystallization is observed by the emergence of new orientations in regions of prior disorder (both in the bulk of the sample and at numerous surface-connected regions). A spatial resolution of several microns allows the analysis of nucleating regions prior to the event in order to search for mechanisms associated with the emergence of specific orientations. Spatial resolution also bounds the average motion of grain boundaries, which in the current work is comparable to the spatial resolution of ≈5 μm.

The ability to observe subtle intragranular orientation structure, such as in Fig. 2, originates from the measurement of many Bragg peaks from arbitrary orientations. An orientation places these peaks in specific ω bins (and, therefore, specific detector images) where the Bragg condition is satisfied. This occurs when the ω rotation orients the reciprocal lattice vector, $\mathbf{G}$, such that $\mathbf{k}_i \cdot \mathbf{G} = -0.5G^2$, where $\mathbf{k}_i$ is the incident X-ray wavevector which is fixed in the laboratory coordinate system, as is the rotation axis. The reciprocal lattice vectors rotate with the sample. Binning ~30 distinct peaks strongly constrains the orientation. If the lattice within a nominal grain rotates by even a fraction of the integration interval, $\delta\omega = 1°$, it is likely that some subset of the scattering will be shifted to different ω intervals. In contrast to simply shifting intensity distributions within the nominal grain's projected images, this shifting to distinct images is easily followed by the voxel-based reconstruction code.

A caveat to literal interpretation of images such as in Fig. 2 is that structure exists on length scales much smaller than the resolution of 5 μm in this work. The orientations deduced from the present diffraction data are, presumably, averages of orientations within the sample space voxels. When sub-resolution orientation variations become too broad, the scattering from a voxel becomes both broad and weak. Lattice rotations about different axes generate anisotropic peak broadening that results in some peaks

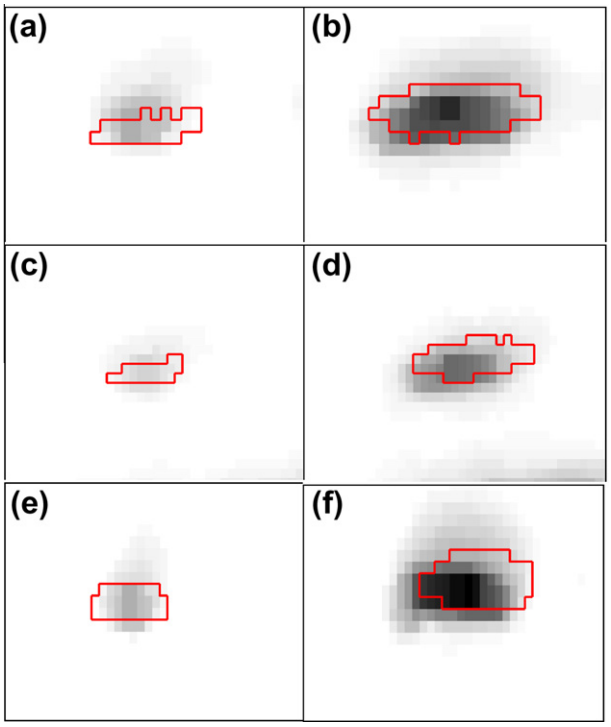

Fig. 6. Bragg scattering generated by the recrystallized grain of Fig. 5. Rows show three distinct peaks using identically sized detector regions, while columns correspond to different anneal states. All images use the same intensity gray scale. Raw experimental data have been filtered and background subtracted. The red outlines define the regions covered by simulated scattering from the reconstructed grain.

Table 1
Misorientation relations of grains in the neighborhood of the nucleated grain. See the text for definitions of grain identifier numbers.

Number	Angle (°)	Axis		
1	14.4	−0.559	−0.822	0.108
2	12.3	−0.585	0.054	−0.809
3	34.3	−0.263	−0.057	−0.963
4	36.7	−0.239	0.068	0.969
5	33.9	−0.554	0.293	0.779
6	24.9	0.012	0.160	0.987
7	40.9	−0.093	0.235	−0.968

falling below the detection limit. In the present data, the confidence measure is seen to drop to low values in particular sample regions. High *KAM* and low *C* can qualitatively indicate "disordered" regions, as we have described here. Similarly, calculations of dislocation content (not performed here) will need to be taken as lower bounds, since the orientation field has been smoothed over the resolution length scale. Future data sets with spatial resolution of the order of at least some cell structures will make such calculations relevant to placing bounds on actual dislocation content and evolution.

With regard to recrystallization, the degree to which general conclusions can be drawn from a single event is certainly limited. Nevertheless, we note the counterintuitive nature of the appearance of new orientations in recrystallization [23]. As discussed above, no evidence for scattering from the orientation of the new internal grain (and from its location) could be identified in the initial state data even when the raw diffraction images were examined. This observation is consistent with a single nucleating grain observed by Larsen et al. [15]. That grain, in a copper sample, is located near a triple junction and has an orientation with no simple relation to the three adjacent grains. Our observation, made possible through more detailed spatial resolution, is that the new grain presented here grows out of a highly disordered region which is surrounded by seven distinct grains. This location possibly avoids the highly unfavorable nucleation threshold for a random orientation in contact with surrounding crystals [23]. Our measurement cannot, of course, say anything about the prior existence of a subcell of appropriate orientation and of a size below our detection threshold. The low *C* region is likely to contain a high concentration of small-scale features; future higher-resolution measurements may be able to address such structures. At the annealing temperatures used here, high-angle ($\geqslant 2°$) boundaries between existing grains elsewhere in the microstructure move very little; therefore, it is not surprising that the nucleated grain does not grow discernibly into existing well-ordered grains. Additional event statistics are clearly needed.

5. Conclusion

An application of forward modeling analysis to nf-HEDM has been presented, demonstrating its ability to characterize subgrain evolution in the annealing of defected polycrystals. Through the combined analysis of reconstructed orientation maps in sample space and diffraction peak characterization in detector space, we are able to identify and validate salient features associated with both microstructure recovery and recrystallization. Intragranular orientation variations that reflect geometrically necessary dislocation structures are observed to evolve toward more uniform orientations both below and above the 5 μm spatial resolution limit of this measurement. The growth of new, well-ordered grains from disordered regions of the sample is observed both in bulk and at the sample surface. All observations are based on 3-D structures deduced from extensive data sets that include many Bragg peaks from each sample region and crystallographic orientation. The non-destructive nature of the measurement allows for the possibility of looking at regions in which critical events or slowly evolving structural changes occur in sample treatment states prior to the events. This retrospective ability eliminates the "lost evidence problem" associated with critical events, such as nucleation [24]. The examination of specific microstructural regions of interest as seen in the reconstructions is complemented by examination of detector regions that are highlighted by the reconstruction software.

The measurements reported here were carried out in 2007. Since that time, many improvements in beamline hardware at the APS have been implemented. Data collection has been accelerated to the point where typical volu-

metric data sets of 100 layer measurements are collected in less than 24 h (actual speed depends on signal strength inherent to sample material and its condition). The standard detector system now has 1.5 μm resolution instead of the 5 μm pixels and resulting grid resolution used here. With the development of continuous scanning, integration intervals $\delta\omega < 1^\circ$ can be collected without prohibitively increasing data collection time. On the reconstruction side, development is underway to implement explicit matching of simulated intensity distributions to those observed experimentally. Extension of the current work, as well as studies of microstructure evolution due to other driving forces, are in progress.

Note added in proof

On further investigation, we have detected, in the initial, unannealed state, a very weak diffraction signal associated with the orientation and location of the emerging grain of Fig. 5; the signal exists only in a single layer which is adjacent to that shown. With improved signal extraction from the raw images of diffraction peaks and with refined reconstruction parameters, our search algorithm converges to this orientation in a set of disconnected but vicinal voxels located within the low confidence region. The diffraction and reconstruction are consistent with a barely resolved, not yet fully ordered domain within the highly deformed region. Details will be elaborated in the PhD Thesis by C. M. Hefferan, Physics Dept., Carnegie Mellon University.

Acknowledgements

The authors thank D. Hennessy for assistance with data collection. This work was supported primarily by the Metals and Nanostructures and the Materials Research Science and Engineering Center programs of the National Science Foundation under Award Numbers DMR-1105173 and DMR-0520425, respectively. The research was also supported in part by the National Science Foundation through TeraGrid resources provided by Texas Advanced Computing Center under Grant No. DMR080072. Use of the Advanced Photon Source was supported by the US Department of Energy, Office of Science, Office of Basic Energy Sciences, under Contract No. DE-AC02-06CH11357.

References

[1] Humphreys FJ, Hatherly M. Recrystallization and related annealing phenomena. Oxford: Elsevier; 1995.
[2] Poulsen HF. Three-dimensional X-ray diffraction microscopy. Berlin: Springer; 2004.
[3] Suter RM, Hennessy D, Xiao C, Lienert U. Rev Sci Instrum 2006;77:1–12.
[4] Lienert U, Li SF, Hefferan CM, et al. J Miner Metals Mater Soc 2011;63:70–7.
[5] Liu W, Ice GE, Larson BC, Yang W, Tischler JZ. Ultramicroscopy 2005;103:199–204.
[6] Larson BC, Yang W, Ice GE, Budai JD, Tischler JZ. Nature 2002;415:887–90.
[7] Johnson G, King A, Goncalves Honnicke M, Marrow J, Ludwig W. J Appl Crystallogr 2008;41:310–8.
[8] Ludwig W, Schmidt S, Lauridsen EM, Poulsen HF. J Appl Crystallogr 2008;41:302–9.
[9] Ludwig W, Reischig P, King A, Herbig M, Lauridsen EM, Johnson G, et al. Rev Sci Instrum 2009;80:1–9.
[10] Gundlach C, Pantleon W, Lauridsen EM, Margulies L, Doherty RD, Poulsen HF. Scr Mater 2004;50:477–81.
[11] Lauridsen EM, Juul Jensen D, Poulsen HF, Lienert U. Scr Mater 2000;43:561–6.
[12] Offerman SE, van Dijk NH, Sietsma J, et al. Science 2002;298:1003–5.
[13] Lauridsen EM, Poulsen HF, Nielsen SF, Juul Jensen D. Acta Mater 2003;51:4423–35.
[14] Schmidt S, Nielsen SF, Gundlach C, Margulies L, Huang X, Juul Jensen D. Science 2004;305:229–32.
[15] Larsen AW, Poulsen HF, Margulies L, Gundlach C, Xing Q, Huang X, et al. Scr Mater 2005;53:553–7.
[16] Lauridsen EM, Schmidt S, Nielsen SF, Margulies L, Poulsen HF, Juul Jensen D. Scr Mater 2006;55:51–6.
[17] Rollett AD, Lee S-B, Campman R, Rohrer GS. Annu Rev Mater Sci 2007;37:627–58.
[18] Hefferan CM, Li SF, Lind J, Suter RM. Powder Diffr 2010;25:132–7.
[19] Hefferan CM, Li SF, Lind J, Lienert U, Rollett AD, Wynblatt P, et al. Comput Mater Continuat 2009;14:209–19.
[20] Li SF. PhD thesis, Carnegie Mellon University, 2011.
[21] Weissmann S. Characterization of lattice defects and concomitant strain distribution. In: Barrett CS et al., editors. Advances in X-ray analysis, vol. 35A. New York: Plenum Press; 1992.
[22] Brewer LN, Field DP, Merriman CC. Mapping and assessing plastic deformation using EBSD. In: Schwartz AJ et al., editors. Electron backscatter diffraction in materials science. New York: Springer Science; 2009.
[23] Doherty RD et al. Mater Sci Eng A 1997;238:219–74.
[24] Duggan B. ICOTOM 11, 1996; as quoted in [15].